

Photocatalytic removal of tetracycline by a Z-scheme heterojunction of bismuth oxyiodide/exfoliated g-C₃N₄: performance, mechanism, and degradation pathway

Hui Liu ^a, Wangchen Huo ^b, Tian C. Zhang ^c, Like Ouyang ^{a,*,**}, Shaojun Yuan ^{a,*}

^a Low-carbon Technology & Chemical Reaction Engineering Lab, School of Chemical Engineering, Sichuan University, Chengdu 610065, China

^b Guangdong-Hong Kong-Macao Joint Laboratory for Contaminants Exposure and Health, Guangdong Key Laboratory of Environmental Catalysis and Health Risk Control, Institute of Environmental Health and Pollution Control, Guangdong University of Technology, Guangzhou 510006, China

^c Civil and Environmental Engineering Department, University of Nebraska-Lincoln, Omaha, NE 68182-0178, USA



ARTICLE INFO

Article history:

Received 5 October 2021

Received in revised form

23 November 2021

Accepted 3 December 2021

Available online 7 January 2022

Keywords:

Z-scheme heterojunction

BiOI

g-C₃N₄

Photocatalysis

Tetracycline degradation

ABSTRACT

Antibiotics, once being released into the environment, become recalcitrant organic pollutants, which pose a potential risk to ecological balance and human health. In this study, a Z-scheme heterojunction of bismuth oxyiodide (BiOI)/exfoliated g-C₃N₄ (BiOI/ECN hereafter) was synthesized by the combination of thermal exfoliation of g-C₃N₄ and chemical precipitation of BiOI for efficient photocatalytic degradation of tetracycline in aqueous solutions under visible light irradiation. The optimized BiOI/ECN delivered an outstanding degradation rate at circa 0.0705 min⁻¹, which was 10 times higher than that of the bulk g-C₃N₄. The photocatalytic degradation efficiency of tetracycline remained almost unchanged in a pH range of 3–11, and the BiOI/ECN displayed an excellent photostability upon recycled usage. The photocatalytic mechanism of tetracycline was ascribed to the main reactive oxidation species of photogenerated holes and superoxide radicals. In addition, the possible degradation pathways of tetracycline were investigated by HPLC-MS to identify intermediates. The toxicity of photocatalytic-generated intermediates of tetracycline was found significantly alleviated according to the calculation of quantitative structure–activity relationship prediction. This work not only provides an attractive photocatalyst for the removal of tetracycline but also opens a new avenue for rational design of Z-scheme heterojunction composites for tetracycline degradation.

© 2021 Elsevier Ltd. All rights reserved.

1. Introduction

Tetracycline (TC) is an antibiotic drug commonly applied to the treatment and prevention of human and animal diseases because of its low cost and satisfactory antibacterial activity [1,2]. However, only a small part of the antibiotics can work in the body, a considerable part (30%–90%) will be excreted through urine and feces into the environment and be detected in the form of prototype or metabolites in various environmental substrates [3–5]. Thus, these residual compounds present a potential hazard to the ecosystem and public health and safety.

Various traditional methods, for example, adsorption [6], membrane processes [7], and biodegradation [8], have been proven

to be effective in removing TC from the environment. Nevertheless, they have not been widely applied because of their low removal efficiency and long treatment period. Photocatalytic technology makes good use of the inexhaustible sunlight to stimulate photocatalytic reactions to generate free radicals, which can oxidize and decompose organic contaminants into some smaller molecules. The advantages of high removal rate, complete mineralization of most toxic compounds, and harnessing solar energy make the photocatalytic technology a promising technology for wastewater treatment [9,10].

Graphitic carbon nitride (g-C₃N₄) is a novel non-metallic semiconductor photocatalyst with a suitable band gap of 2.7 eV, which is responsive to visible light. Moreover, some other unique characteristics, including facile preparation, environmental friendliness, and high stability, make it attract more attentions in the environmental field [3,11]. However, the bulk g-C₃N₄ often possesses small specific surface area and suffers from serious

* Corresponding author.

** Corresponding author.

E-mail addresses: like.ouyang@scu.edu.cn (L. Ouyang), ysj@scu.edu.cn (S. Yuan).

charge recombination, thus limiting its practical application. The exfoliation of g-C₃N₄ is an easy and beneficial way to overcome these shortcomings because it can increase the specific surface area and shorten the migration path of photogenerated carriers [12,13]. Beyond that, several studies have demonstrated that fabricating a heterojunction structure with other semiconductors such as Sn₃O₄ [3], MoS₂ [14], BiVO₄ [15], and ZnO [16] is an effective way to regulate the photocatalytic property of g-C₃N₄. Particularly, the construction of Z-scheme heterojunction can promote the separation of photogenerated carriers while retaining the strong reducibility and oxidizability [17].

Bismuth oxyiodide (BiOI), with an estimated band gap of 1.8 eV, is endowed with superior absorption ability in the visible light region. The layered tetragonal crystal structure is built by the alternative stacking of [Bi₂O₂]²⁺ layers and slabs of iodine atoms. This two-dimensional layered structure can form an internal electrostatic field in BiOI, which contributes to the migration and separation of photogenerated carriers [18]. The adsorption process has an important effect on the occurrence of redox reactions, which can enhance the contact between contaminants and the catalytic center, thus influencing the photocatalytic efficiency. Recently, it has been reported that BiOI had highly adsorptive capacity for toxic metal ions and organic pollutants besides possessing remarkable photocatalytic performance [19–21]. Many studies have successfully designed and prepared a heterojunction structure composed of BiOI and other semiconductors to improve photocatalytic performance [19,22,23]. The energy level of BiOI can match well with g-C₃N₄, and the relatively positive valence band position of BiOI can provide photogenerated holes with higher oxidation capacity for the oxidation and degradation of pollutants. Therefore, we anticipate that the highly efficient removal of TC can be achieved by the rational design of the BiOI/exfoliated g-C₃N₄ (ECN) Z-scheme heterojunction composite. It has been previously reported that BiOI/g-C₃N₄/CeO₂ [24] and g-C₃N₄/BiOI/ β -phase polyvinylidene fluoride membrane (PVDF) photocatalytic membranes [25] had high photocatalytic performance for the degradation of TC under visible light irradiation. In practical applications, the photocatalytic degradation process is very complex, which is affected not only by the photocatalysts but also by some key environmental factors, such as pH values, coexisting ions, pollutant concentration, and so on. However, few reports have been explored so far. In addition, the photodegradation intermediate products of TC and photocatalytic mechanisms of BiOI/g-C₃N₄ system have been rarely reported. Therefore, it is necessary to systematically investigate the photocatalytic performance, reaction mechanism, and intermediate products of the photodegradation of TC for BiOI/g-C₃N₄ system under visible light irradiation.

Herein, Z-scheme BiOI/ECN heterojunctions with various BiOI loading amounts were prepared by a simple chemical precipitation method. Multiple characterization techniques were used in studying chemical compositions, microstructures, and photoelectric properties of the as-fabricated photocatalysts. The photocatalytic performance was assessed by the visible light-driven photocatalytic degradation of TC. Considering the practical application, the impacts of different factors, including catalyst dosages, concentrations of TC, pH values, and coexisting ions, were investigated. Subsequently, the photocatalytic mechanism was explored through the active species trapping experiment, electron spin resonance (ESR) testing, and the density functional theory (DFT) calculation. Finally, the main intermediates were identified, and the possible degradation pathways of TC using the BiOI/ECN photocatalyst were proposed. The quantitative structure–activity relationship (QSAR) prediction was used to evaluate the toxicity of the intermediates.

2. Experimental section

2.1. Materials

Melamine was supplied by Shanghai Aladdin Bio-chem. Technol. Co. (Shanghai, China). Other chemical reagents, including Bi(NO₃)₃·5H₂O, KI, NaOH, HNO₃, NaCl, NaNO₃, Na₂SO₄, Na₂CO₃, Mg(NO₃)₂, Ca(NO₃)₂, ethylene glycol (EG), and ethanol, were all purchased from Kelong Chemical Co. (Chengdu, China). TC was obtained from Titan Scientific Co. (Shanghai, China). All chemical reagents used in this study were of analytical grade and could be used directly without any treatment. The deionized (DI) water (18.25 M Ω ·cm) produced by a water purification system was used in the whole process.

2.2. Preparation of Z-scheme BiOI/ECN photocatalyst

Scheme 1 illustrated an overview of the fabrication process of the novel photocatalysts. Bulk g-C₃N₄ was obtained from a conventional thermal polycondensation method. Briefly, an open crucible containing 5 g of melamine was put into a tube furnace (OTF-1200X, HF-Kejing, China) and then heated to 550°C for 4 h with a ramping rate of 20°C/min under the air ambience. After the yellow product was cooled naturally, it was collected and ground into powder with an agate mortar. The previously mentioned product was named as “BCN.” After further thermal treatment, the ECN was synthesized [12]. Briefly, 0.5 g of BCN was calcined at 550°C for 3 h with a heating rate of 20°C/min in the air. The obtained light-yellow powder was marked as “ECN” and collected for future use.

The BiOI/ECN composites were fabricated via a chemical precipitation method as follows. A certain quantity of Bi(NO₃)₃·5H₂O and 0.2 g of ECN were poured into 30 mL of ethylene glycol, and the mixture was ultrasonically dispersed for 1 h with a KQ-400DE ultrasonic cleaner (KunShan Ultrasonic Instruments Co., China). Thirty milliliters of KI aqueous solution (the molar ratio of KI to Bi(NO₃)₃·5H₂O is 1) was slowly added to the previously mentioned mixture and then stirred for 5 h at room temperature. The tangerine precipitate was centrifuged and washed with DI water and ethanol at 5,000 rpm for several times, and then the sediments collected by the centrifuge tubes were dried overnight in an oven at 60°C. The resulting powder was named as “BiOI/ECN-x,” in which x stands for the ratio of the theoretically generated mass of BiOI to the mass of the added ECN. In addition, pure BiOI was synthesized using the same procedure as described previously, but without the addition of ECN.

2.3. Characterization

The X-ray diffraction (XRD) data were characterized by a DX2700 X-ray diffractometer from Haoyuan Instruments Co. ($k = 1.5418 \text{ \AA}$, Cu K α radiation). The Fourier transform infrared (FT-IR) spectra were determined by the standard KBr disk method on a L1600300 spectrometer (PerkinElmer Inc., USA). The scanning electronic microscopy (SEM) and energy dispersive spectrometry (EDS) mapping were recorded by a JEOL JSM-7610 SEM (Toyoko, Japan). Transmission electron microscopy (TEM) images were collected by a TEM of Tecnai G2 F20 S-TWIN (FEI Co. OR, USA). The X-ray photoelectron spectra (XPS) were obtained by a Thermo Scientific K-Alpha spectrometer (ThermoFisher, USA). The ultraviolet–visible diffuse reflectance spectra (UV–vis DRS) were carried out on a Perkin Elmer Lambda 750S spectrometer. The photoluminescence (PL) spectra were performed on an FLS920 spectrometer of Edinburgh Instruments (UK), which was equipped with an X 900 lamp for excitation at room temperature. The Zeta potentials of the photocatalyst were recorded on a Zetasizer Nano

ZS90 potential analyzer (Malvern Panalytical, UK). The ESR spectra were measured by a MiniScope MS-5000X (Magnetech, Germany) spectrometer, and the probe used in the tests was 5,5-dimethyl-L-pyrroline N-oxide (DMPO). A liquid chromatography-mass spectrometry (LC-MS) system (LCMS-8040, Shimadzu, Japan) was used for identifying the products in residual TC solution. The mobile phase was consisted of 70% methanol aqueous solution, and 2 μL was the volume for each injection. The positive ionization mode with an electrospray ionization source was applied to test.

2.4. Photocatalytic performance of the photocatalysts toward TC

The photocatalytic performance of the as-fabricated BiOI/ECN photocatalysts was evaluated by degrading TC. The 500 W xenon lamp (CEL-HXF300-T3, CEALIGHT, Beijing, China) was selected as the light source used in the experiments, and it was equipped with a 420 nm cutoff filter. The photocatalytic reaction happened in a 100 mL jacketed reactor connected with a circulating cooling water system to maintain the reaction temperature at 25°C. Fifty milligrams of photocatalyst and 50 mL of 20 mg/L TC aqueous solution were poured into the reactor being tightly wrapped in a tin foil paper. Under the shading condition, the mixture was stirred continuously to make TC molecules achieve the equilibrium of adsorption and desorption on the catalyst. Three milliliters of test solution was sampled, and the catalyst was filtered out through a 0.22- μm Millipore filters before testing. The residual concentration of TC in the filtrate was determined by TU-1810PC UV-vis spectrophotometer (Purkinje General Instrument Co., Beijing, China) at 357 nm.

The photocatalytic activity testing under different conditions such as solution pH, coexisted ions, the regeneration, and recycle use of photocatalysts as well as the free radical trapping experiments are presented in detail in the [Electronic Supporting Information \(ESI\) S1.1-S1.4](#), respectively.

2.5. Photoelectrochemical properties of the photocatalysts

The electrochemical impedance spectroscopy (EIS) and transient photocurrent response were both measured at the CHI-660E

(Chenhua Instruments, China) electrochemical workstation. The detailed procedures were described in the ESI S1.5.

2.6. Computational studies

Herein, the Vienna ab initio simulation package (VASP) was used in the process of DFT calculations [26]. The interactions between the ions and electrons were described by the projector augmented wave method [27], and the Perdew-Burke-Ernzerhof exchange correlation function using the generalized gradient approximation (GGA) was used to all geometry optimizations [28], where the relaxations convergence criteria were 0.01 eV/Å and 10^{-5} eV. In addition, the plane-wave kinetic energy cutoff was set to 500 eV, and the uniform Gamma-centered k-point grid in the Brillouin zone was set to $2\pi \times 0.03 \text{ \AA}^{-1}$ via using the VASP codes [29]. The Van der Waals correction (DFT + D3) was applied to treat the interaction between layers of g- C_3N_4 [30,31]. Based on the XRD and high-resolution TEM (HRTEM) analyses, the slabs of BiOI and g- C_3N_4 with 15 Å of vacuum space used to calculate the work function were cut along the 110 facets and 001 facets, respectively. To calculate the more exact electronic structure, the Heyd-Scuseria-Ernzerhof (HSE06) hybrid exchange correlation function was used in band structure and density of states (DOS) simulation [32].

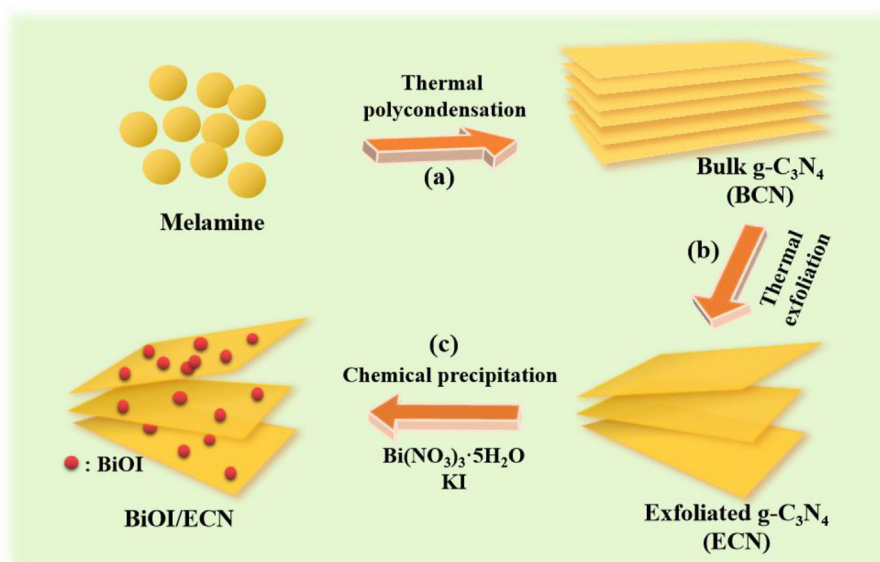
2.7. Toxicity evaluation of photocatalytic-generated TC intermediates

The details of the method for evaluating the toxicity of photocatalytically generated TC intermediates can be seen in ESI S1.6.

3. Results and discussion

3.1. Characterization of the heterojunction BiOI/ECN photocatalysts

Fig. 1a displays the XRD to ascertain the phase and crystal structure of the as-fabricated photocatalysts. As can be seen from the pattern, BCN has two typical diffraction peaks. The peak at 13.1° corresponding to the (100) crystal plane is attributed to the interplanar packing of heptazine units, whereas the other peak centered at 27.7° belongs to the (002) plane of g- C_3N_4 , which is associated



Scheme 1. Schematic diagram of the fabrication process of the BiOI/ECN composite: (a) fabrication of bulk g- C_3N_4 (BCN) via thermal polycondensation method; (b) preparation of exfoliated g- C_3N_4 (ECN) via thermal treatment; and (c) synthesis of BiOI/ECN composite via chemical precipitation method.

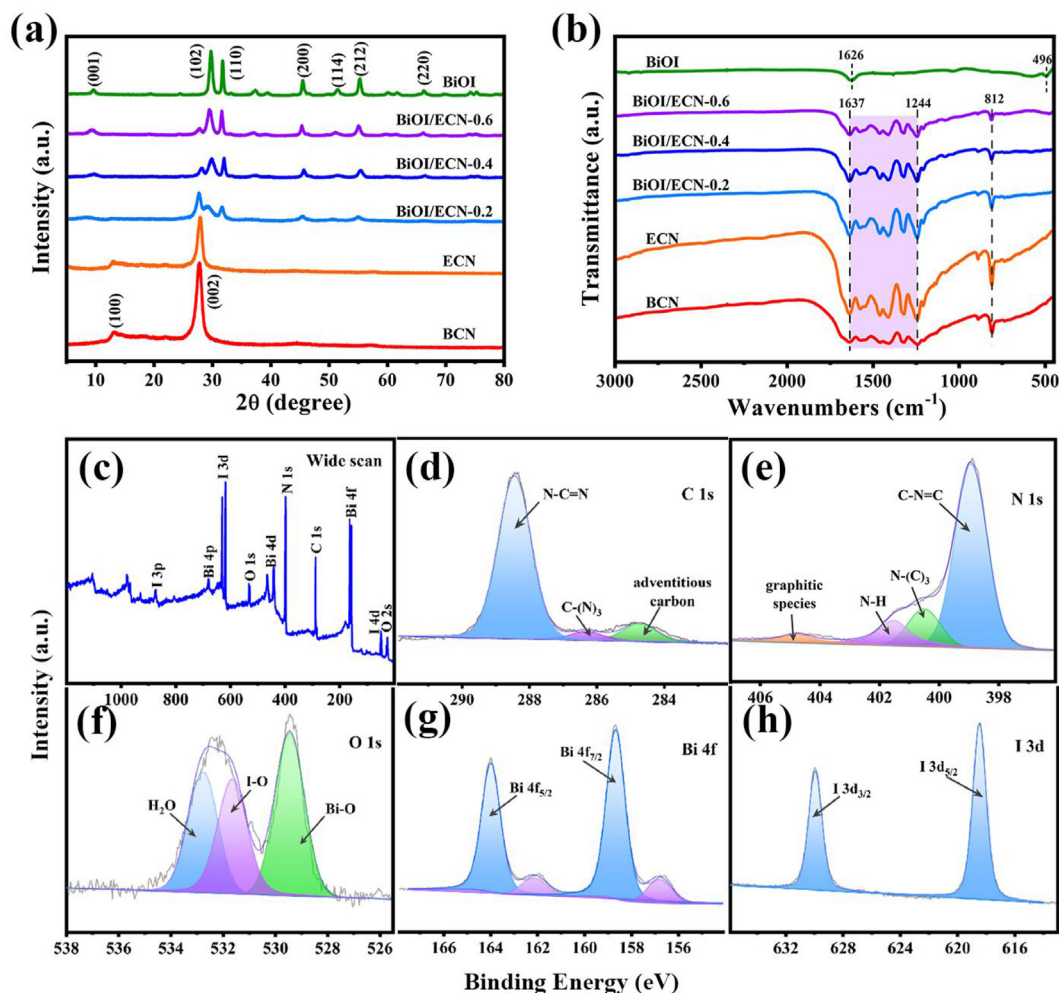


Fig. 1. (a) XRD patterns and (b) FT-IR spectra of the samples prepared. XPS spectra of the BiOI/ECN-0.4 composite: (c) wide scan, (d) C 1s, (e) N 1s, (f) O 1s, (g) Bi 4f, and (h) I 3d.

with interlayer stacking of aromatic rings [33]. The XRD pattern of ECN is not much different from that of BCN, revealing the thermal stability of its crystal structure. Specifically, the peak (002) of ECN becomes weaker and moves from 27.7° to 27.9° (ESI, Fig. S1). The results indicate that ECN exhibits less numbers of aligned layers and the reduced gallery distance between layers, demonstrating the successful exfoliation of BCN [12,34]. The XRD pattern for pure BiOI has several peaks that could be well matched with the tetragonal phase (JCPDS No. 10-0445). For the BiOI/ECN composites, characteristic diffraction peaks of two pure substances are observed, which demonstrates the successful preparation of the composites. In addition, as the content of BiOI increases, the peaks belonging to BiOI become stronger, indicating that more BiOI is combined with ECN.

The results of FT-IR are shown in Fig. 1b. As for the BiOI, the absorption band at 496 cm^{-1} is ascribed to the stretching vibration of the Bi–O in BiOI, and the peak centered at $1,626\text{ cm}^{-1}$ is assigned to O–H bending vibration of water [18]. Except for the spectrum of BiOI, the sharp peak at 812 cm^{-1} originates from the breathing mode of triazine units, and the peaks at $1,244$ – $1,637\text{ cm}^{-1}$ refer to the typical stretching vibration modes of C–N heterocycles [14]. Compared with BCN, ECN shows similar peak features, but the intensity is increased significantly, indicating that the arrangement of tri-s-triazine units is more orderly [35]. The peaks of BiOI are much weaker than that of ECN. Thus, the BiOI/ECN composites show

almost similar characteristics as ECN. Moreover, the structure of ECN was not destroyed after incorporating with BiOI.

Fig. 1c–h present the XPS spectra of the BiOI/ECN-0.4 composite, which provides insight into the elemental species and chemical states of the sample. The wide scan XPS spectra shown in Fig. 1c demonstrate that the BiOI/ECN-0.4 composite is made up of C, N, Bi, I, and O, without impurity elements. In detail, the three main peaks of C 1s spectrum at about 288.4 eV , 286.3 eV , and 284.7 eV should be attributed to N=C=N, C-(N)₃ and adventitious carbon species, respectively (Fig. 1d) [36]. The N 1s spectrum is divided into four characteristic peaks (Fig. 1e), which could be assigned to the graphitic species (404.8 eV), N–H (401.5 eV), N-(C)₃ (400.5 eV), and C–N=C (398.9 eV), respectively [37,38]. In Fig. 1f, the peak at 532.8 eV is considered as H₂O molecules adsorbed on the surface of the composite [39], whereas the peak at 531.7 eV is due to I–O bonds, and the peak at 529.5 eV is the characteristic Bi–O bonds in [Bi₂O₂] slabs of BiOI [40,41]. Fig. 1g shows two typical peaks at 164.0 and 158.7 eV , which are Bi 4f_{5/2} and Bi 4f_{7/2} for Bi³⁺ in BiOI, respectively [22]. Fig. 1h shows that the characteristic peaks of I 3d at 629.9 eV and 618.5 eV belong to I 3d_{3/2} and I 3d_{5/2}, indicating the chemical state of I in the composite is of -1 valence [41,42]. Combining the results of FT-IR and XRD, it can be proven that the BiOI/ECN-0.4 composites were successfully prepared.

SEM was carried out to further explore the microstructure of the samples. Fig. 2a shows a loose layered stacked structure of ECN,

which may be beneficial to increase the active sites for adsorbing pollutant molecules. On loading BiOI, some fragments could be evidently noticed on the surface of ECN (Fig. 2b), confirming that the BiOI are well coupled with the ECN.

The TEM image of BiOI/ECN-0.4 in Fig. 2c exhibits BiOI fragments are irregularly scattered on the ECN. The HRTEM image shown in Fig. 2d is further used to reveal the presence of BiOI. The lattice spaces are measured as 0.915 and 0.302 nm, which correspond to (001) and (102) planes of the tetragonal phase of BiOI, respectively [43,44]. These lattice planes are also shown in the XRD results. However, no lattice fringes of *g*-C₃N₄ can be clearly detected because of its low crystallinity [44,45]. Furthermore, the elemental mapping and the corresponding EDS spectrum shown in Fig. 2e–f demonstrate C, N, Bi, I, and O elements coexist in BiOI/ECN-0.4 composite without any other elements. All the aforementioned results illustrate that BiOI has been successfully loaded on the *g*-C₃N₄.

3.2. Photoelectrochemical properties of the BiOI/ECN photocatalysts

Fig. 3a shows the maximum light absorption boundary of ECN located at around 460 nm, whereas stronger visible light absorption of BiOI appears at about 650 nm. A progressive redshift in the absorption edge can be observed as the content of BiOI gradually increased, along with the gradual darkening of the color of the composites (inset in Fig. 3a). The optical band gap energy of ECN and BiOI calculated by Kubelka-Munk formula are circa 2.70 eV and 1.90 eV, respectively, which are consistent with the data presented in the literature [43]. The band gap of ECN is larger than that of BCN because of the quantum confinement effect produced by the decrease in the thickness of internal stacked layers [12,46].

The photocurrent responses can intuitively reflect the separation ability of photoinduced carriers [47]. As it can be seen in Fig. 3c, the photocurrent density of BiOI/ECN composites increases in relative to ECN and BiOI, and the BiOI/ECN-0.4 exhibits the strongest photocurrent response, indicating that the BiOI/ECN composites possess a

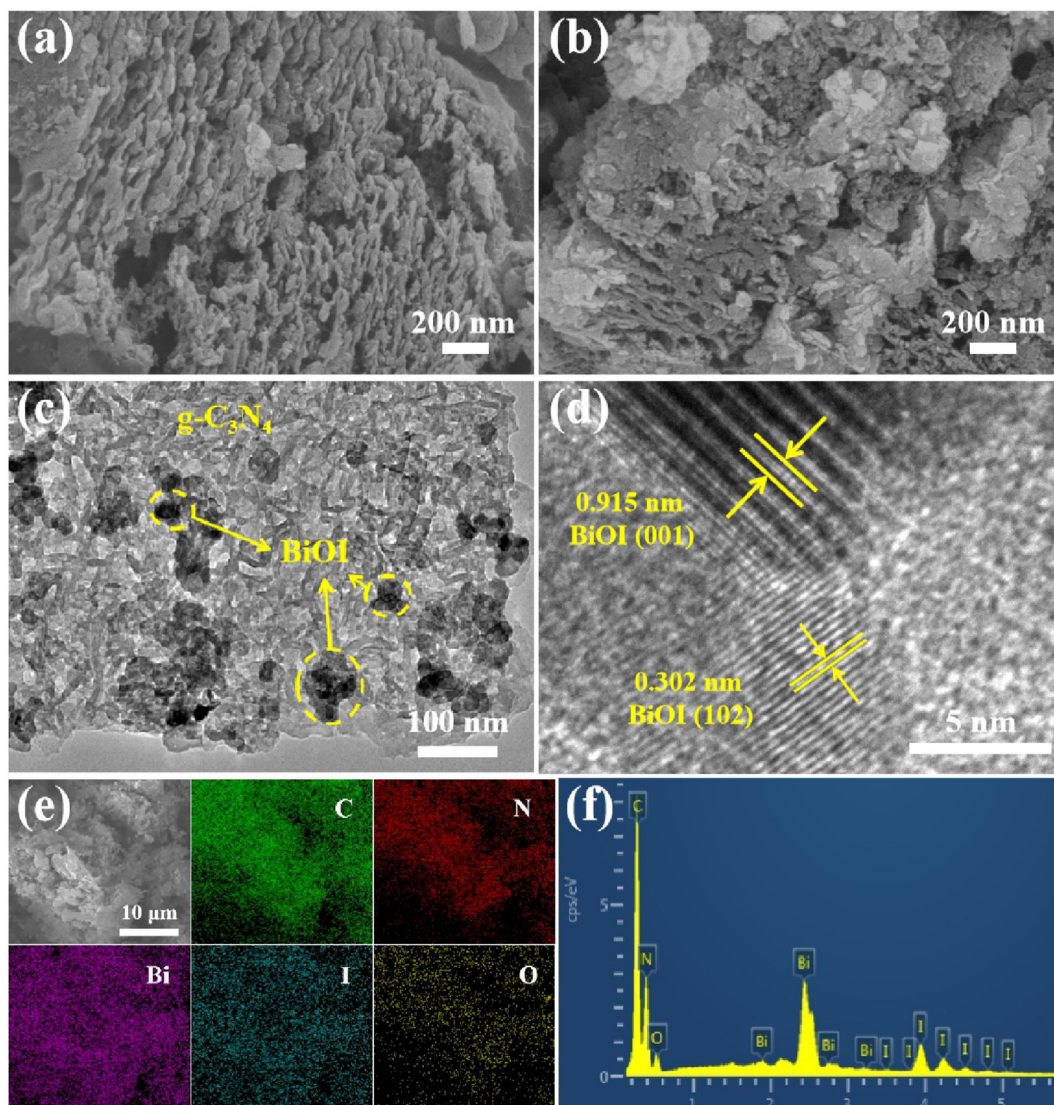


Fig. 2. SEM images of as-fabricated (a) ECN and (b) BiOI/ECN-0.4. (c) TEM and (d) high-resolution TEM images of BiOI/ECN-0.4. (e) The elemental mapping of C, N, Bi, I, and O elements and (f) the corresponding EDS spectrum of BiOI/ECN-0.4 composite.

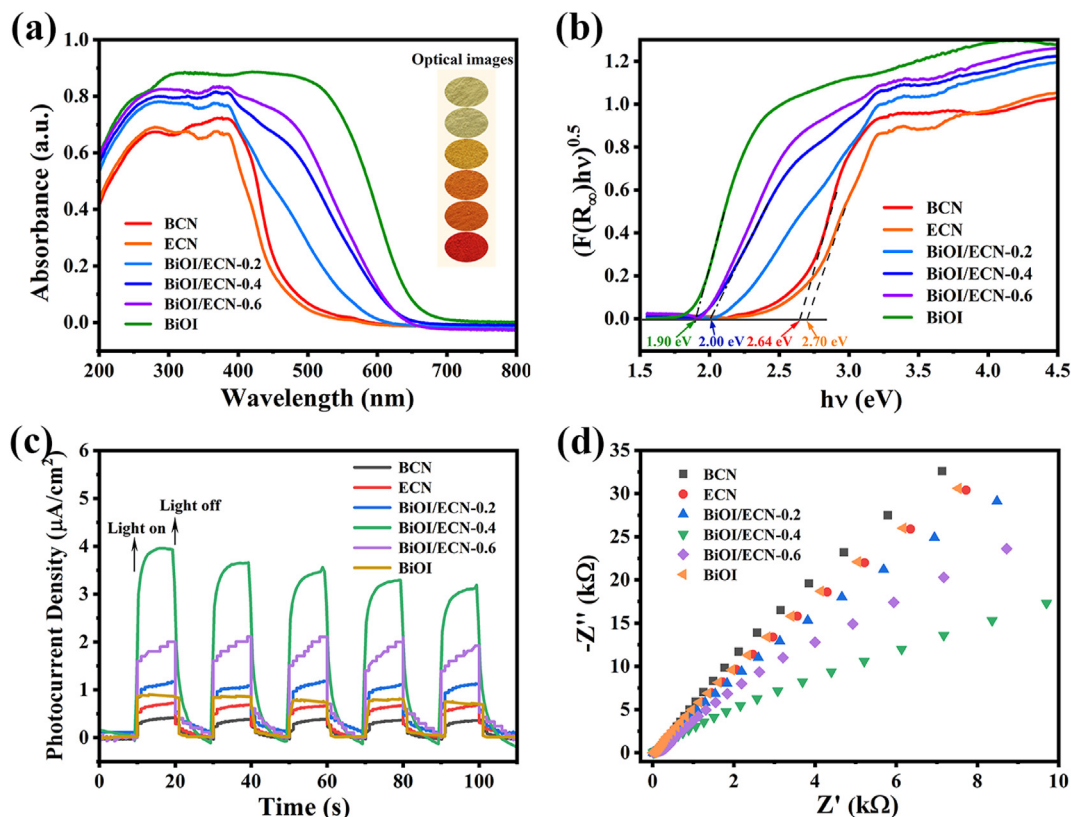


Fig. 3. Optical properties of samples: (a) UV–vis diffuse reflectance spectra, the inset picture is optical images of samples (from top to bottom, they are BCN, ECN, BiOI/ECN-0.2, BiOI/ECN-0.4, BiOI/ECN-0.6, and BiOI) and (b) computing spectral plot of the corresponding samples. Characterizations for the electrochemical property: (c) photocurrent response density and (d) electrochemical impedance spectra.

higher photogenerated electron migration rate and a lower recombination rate of photogenerated carriers, thereby improving the photoactivity. It is well acknowledged that the radius of the arc is proportional to the impedance value in the EIS spectrum. The small radius of arc indicates the high migration efficiency of carriers in the sample [48]. To further explore the transfer of photogenerated charges in photocatalysts, EIS tests were performed (Fig. 3d). It can be clearly observed that BiOI/ECN-0.4 exhibits a smaller radius of arc than those of other samples, suggesting a fast interfacial charge transfer rate of the BiOI/ECN composites. Based on the previously mentioned results, there is no doubt that BiOI/ECN composites exhibit the favorably enhanced visible-light photocatalytic performance by tight contact of ECN and BiOI.

3.3. Photocatalytic performance of the BiOI/ECN photocatalysts toward TC

The photocatalytic performance of the BCN, ECN, BiOI, and different proportions of BiOI in BiOI/ECN composites was evaluated by the ability to remove TC under visible light. As Fig. 4a shows, all the catalysts reached the adsorption and desorption equilibrium during the 30-min of darkness. Therefore, the 30-min dark reaction was used in the following experiments. TC is very stable, and self-degradation hardly takes place without the presence of photocatalyst. Only approximately 25.8% of TC is removed in 30 min over BCN, and the degradation efficiency of TC increases to 62.1% over ECN after thermal treatment. Obviously, the BiOI/ECN composites can significantly enhance the degradation efficiency of TC. Among them, the BiOI/ECN-0.4 composite shows the highest photocatalytic degradation efficiency of TC at circa 86.0% in 30 min. The

reason why the content of BiOI is not proportional to the degradation efficiency may be that too much BiOI accumulates on the surface of ECN, which hinder the electron transfer and retard the separation of photoinduced carriers. In addition, excessive BiOI may provide additional recombination centers for photogenerated electrons and holes, thus affecting the photocatalytic performance. The experimental results are consistent with the results of photocurrent response and EIS testing that BiOI/ECN-0.6 sample has a smaller photocurrent density and a larger arc radius of impedance spectra than those of the corresponding BiOI/ECN-0.4 samples (Fig. 3c and d). It could be found that the degradation efficiency of TC is only 72.7% when BiOI and ECN are physically mixed in proportion, which is lower than 86.0% over BiOI/ECN-0.4 composite. This demonstrates the formation of heterojunction between BiOI and ECN, and there was a certain interaction between them, which promotes the improvement of photocatalytic performance. In addition, the photocatalytic activity curve of BiOI only shows that BiOI has a good adsorption capacity for TC. The specific surface areas of BiOI/ECN-0.4 composite and ECN are determined to be approximately 115.2 and 58.0 m^2/g , respectively (ESI, Fig. S4). This may be ascribed to the changes in ECN structure caused by the introduction of BiOI. However, it is clearly observed that BiOI/ECN-0.4 has a stronger adsorption capacity in the dark condition (Fig. 4a), which further indicates that the addition of BiOI can provide more abundant active sites and adsorb more reactant molecules.

Fig. 4b depicts the pseudo-first-order reaction model was used to investigate the kinetic behaviors of TC degradation over different photocatalysts, and Table S2 lists the corresponding fitted data. The reaction kinetics of TC degradation were well fitted by the model of

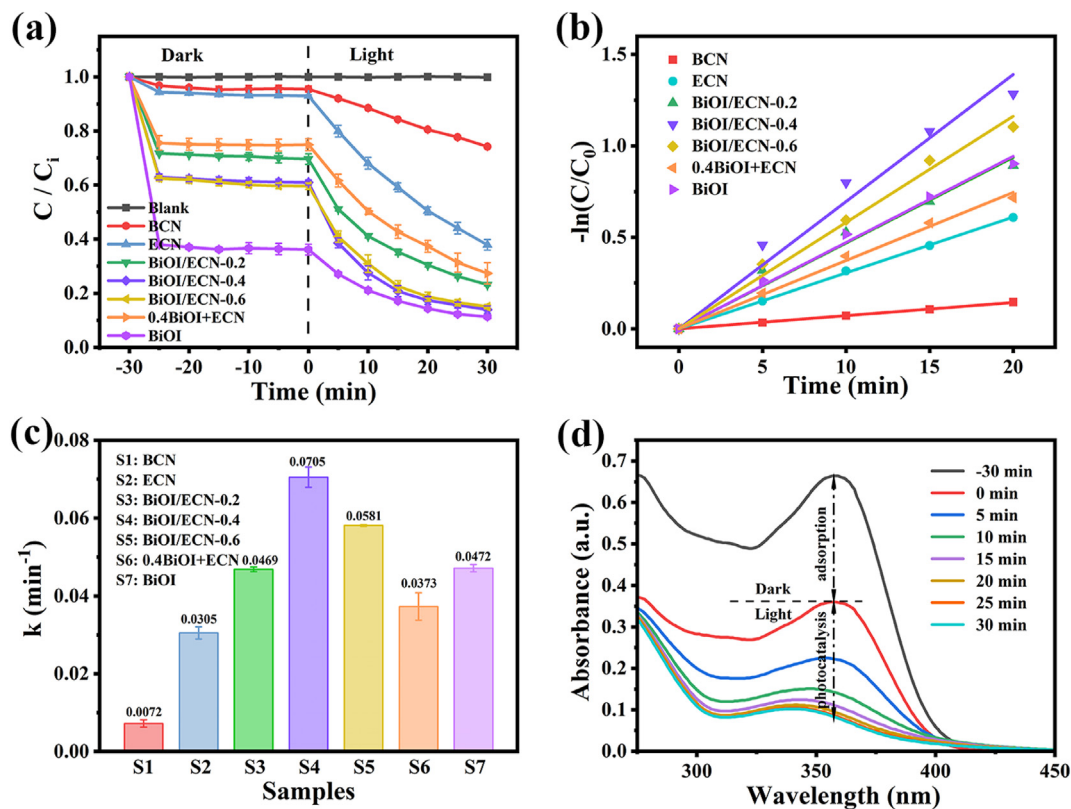


Fig. 4. (a) Photocatalytic activities for degradation of tetracycline under visible light irradiation; (b) the pseudo-first-order kinetics fitted curves; (c) apparent rate constants for tetracycline degradation over different photocatalysts. (d) UV-vis spectra of tetracycline solution for BiOI/ECN-0.4 composite at different irradiation times. The 0.4BiOI + ECN sample in the figures represents a proportional physical mixture of BiOI and ECN, where the mass of BiOI accounts for 40% of ECN. Experimental conditions: $C_1 = 20 \text{ mg/L}$, $C_c = 1.0 \text{ g/L}$, $\text{pH} = 6$, $T = 298 \text{ K}$, and the operating current of the visible light source = 12 A. (C_0 is the initial concentration of tetracycline and C_c is catalyst dosages.)

$-\ln(C/C_0) = kt$ [49], in which C_0 is the concentration at time 0, C is the concentration at time t , and k is the reaction rate constant. It is obvious from Fig. 4c that the BiOI/ECN-0.4 exhibits the highest k value of 0.0705 min^{-1} , which is higher by circa 10 and 2 times than those of BCN at 0.0072 min^{-1} and BiOI at 0.0472 min^{-1} , respectively. The experimental results indicate that the photocatalytic performance of $g\text{-C}_3\text{N}_4$ has been improved after being compounded with BiOI. The comparison of photocatalytic performance of the as-synthesized BiOI/ECN with the previously reported $g\text{-C}_3\text{N}_4$ -based photocatalysts for TC degradation is summarized up in ESI Table S3. It is clearly observed that the BiOI/ECN-0.4 photocatalyst exhibits a comparable removal efficiency of TC to most of previous photocatalyst and delivers the fastest photodegradation rate, indicating a great potential of the BiOI/ECN photocatalyst in the degradation of antibiotics contaminants.

Furthermore, the UV-vis spectra of TC solution for BiOI/ECN-0.4 composite at different irradiation times are displayed in Fig. 4d. The characteristic absorption peak intensity at 357 nm of TC decreased with the increase of reaction time. It directly suggests that TC molecules were gradually reduced in number and decomposed into other substances in the light process [50].

3.4. The effect of environmental factors on photocatalytic performance

First of all, it is important to determine the optimal dosage of catalyst to ensure the efficient and cost-effective of photocatalytic reaction. It can be observed in Fig. 5a that as the catalyst dosage is gradually increased from 0.3 g/L to 1.5 g/L, the removal efficiency of TC under 30 min irradiation also increases from 45.9% to 89.4%.

Increasing the dosage of the catalyst could provide more reactive sites, thereby generating more active substances and promoting the reaction. However, when the amount of catalyst is increased to a certain extent, the degradation efficiency does not increase significantly, presumably because an increase in the turbidity results in the decrease of light absorption efficiency of catalyst [51,52].

Fig. 5b shows the degradation curves of TC under different initial concentration conditions. It is apparent that the concentration of TC is a significant parameter for the entire photocatalytic degradation process. Under the condition of higher concentration of TC, more intermediates are produced and accumulated in the solution, which compete with the active oxidizing substances produced in the photocatalytic system and inhibit the degradation of TC [15]. In particular, BiOI/ECN-0.4 still has a certain capacity to remove TC with 61.9% degradation efficiency after 30 min irradiation in 50 mg/L of TC solution. Therefore, in the actual high concentration wastewater environment, the illumination time can be appropriately prolonged to remove the pollutant more efficiently.

The influence of the initial pH values is displayed in Fig. 5c. Usually, the pH will influence the species of surface charge on photocatalyst and the existence form of organic compound, thus affecting the adsorption capacity of the photocatalyst to the target pollutant. The production of the oxidation species is also affected by pH values [53,54]. However, in our reaction systems, photocatalytic activity is hardly affected by pH values. The point of zero charge of the BiOI/ECN-0.4 was found at about 5.0 (ESI, Fig. S2). TC is an amphoteric compound with three molecular forms [55]. Cations are the dominant form of TC when pH is less than 3.3. As the pH value increases to 7.68, a large number of zwitterion species are produced. Anions occur when pH is greater than 7.68. This can

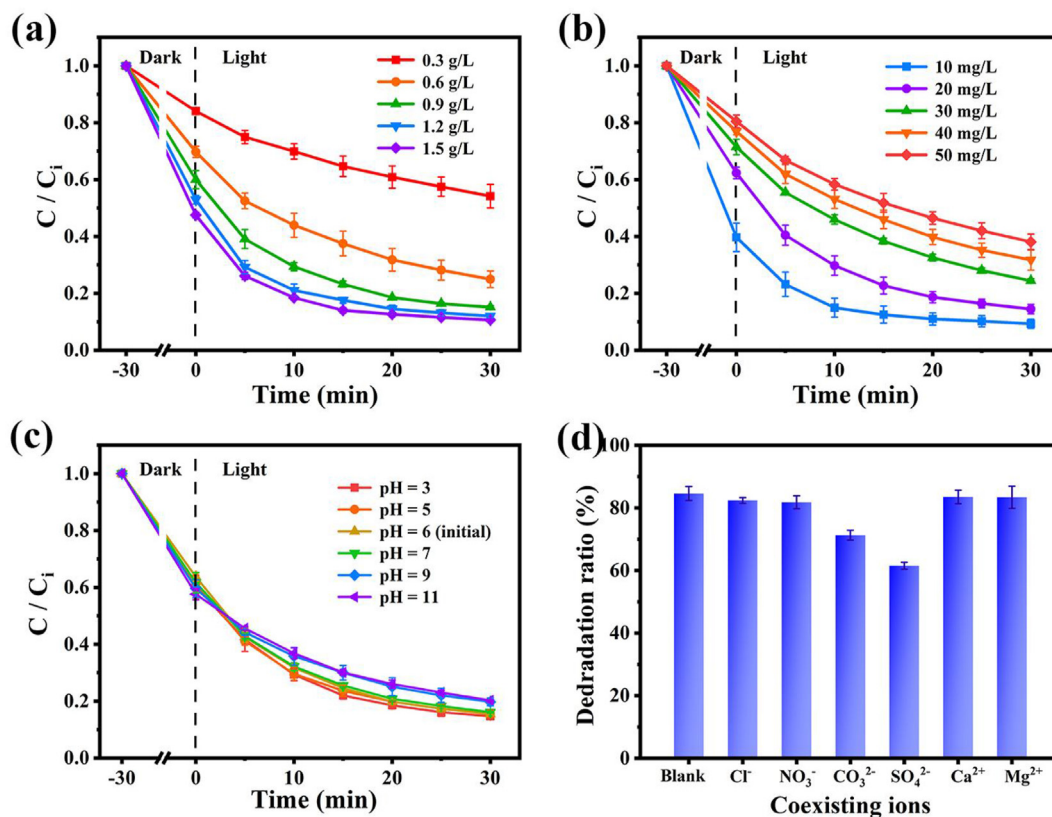


Fig. 5. The impacts of the following factors on the photocatalytic degradation of tetracycline over BiOI/ECN-0.4: (a) catalyst dosages. Experimental conditions: $C_i = 20$ mg/L, $C_c = 0.3$ – 1.5 g/L, pH = 6; (b) initial concentrations of tetracycline. Experimental conditions: $C_i = 10$ – 50 mg/L, $C_c = 1.0$ g/L, pH = 6; (c) initial pH values. Experimental conditions: $C_i = 20$ mg/L, $C_c = 1.0$ g/L, pH = 3–11; and (d) coexisting ions. Experimental conditions: $C_i = 20$ mg/L, $C_c = 1.0$ g/L, pH = 6, $C_{ion} = 5$ mmol/L, [light time] = 30 min. The common conditions: $T = 298$ K, the operating current of the visible light source is 12 A.

explain why the adsorption capacities of TC on the catalyst hardly changes at different pHs. Under alkaline conditions, the removal efficiency of photodegradation TC by BiOI/ECN-0.4 slightly decrease. There are two possible explanations for this result. One is that the catalyst surface is negatively charged, which is not conducive to adsorb hydroxide ions, thus preventing the generation of hydroxyl radicals ($\cdot\text{OH}$). For the other, pH value will have an effect on the formation of oxidation species, and the acidic pH is advantageous to produce photogenerated holes (h^+), whereas neutral or alkaline pH is advantageous to form $\cdot\text{OH}$ [56]. Therefore, h^+ may take a leading role in the TC photodegradation over BiOI/ECN-0.4.

Coexisting ions in practical wastewater are also an important influence factor. Fig. 5d displays the photocatalytic degradation efficiency of TC when there are some general anions (Cl^- , NO_3^- , CO_3^{2-} , and SO_4^{2-}) and cations (Ca^{2+} and Mg^{2+}) in the reaction solution. Compared with the degradation efficiency without the addition of ions, the presence of CO_3^{2-} and SO_4^{2-} exhibits the inhibitory effect, and the introduction of the remaining selected ions negligibly affects the degradation process. The result is caused by the scavenging effect of $\cdot\text{OH}$ and h^+ by these two ions according to the previous reports [57]. Apart from that, the added anions also participate in the competition of pollutant molecules for the active sites on the catalyst surface [58].

3.5. Regeneration and durability of the BiOI/ECN photocatalyst

Fig. 6a shows that although the degradation efficiency of TC decreases to a certain extent after the first run, the photocatalytic

performance is relatively stable in the next five cycles, and the difference between the degradation efficiency in cycle 2 and that in cycle 6 is only 5%. A possible explanation for this might be that the number of adsorption sites of the catalyst is reduced, which would not be conducive to the progress of the photocatalytic reaction. In Fig. 6b–c, the XRD and FT-IR spectrum of the catalyst after six runs are exactly the same as that of fresh sample, indicating that the catalyst shows good chemical stability. Moreover, the fluorescence intensity of the sample after six runs is stronger (Fig. 6d), suggesting that photogenerated carriers have a higher recombination rate. However, the photocatalytic activity is essentially stable, further indicating that the BiOI/ECN-0.4 composite photocatalyst prepared in this study possesses good application potential.

3.6. Photocatalytic mechanism

Fig. 7a shows that the removal efficiency of TC is about 87.5% without the addition of the radical scavengers. The addition of radical scavengers such as IPA, AO, and BQ appears to have some negative impact on the removal efficiency of TC within 30 min. When IPA is added, the photocatalytic activity is not significantly changed, indicating that the hydroxyl free radical ($\cdot\text{OH}$) is not the main oxidizing substance. However, when AO and BQ are used, the photocatalytic degradation processes are significantly inhibited, and the corresponding removal efficiencies decrease to about 40% and 59.4%, respectively. Therefore, photogenerated holes (h^+) and superoxide radicals ($\cdot\text{O}_2^-$) are predominant reactive species for the oxidative degradation of TC, and the influence order of active species is $h^+ > \cdot\text{O}_2^- > \cdot\text{OH}$. The presence of oxidative species is

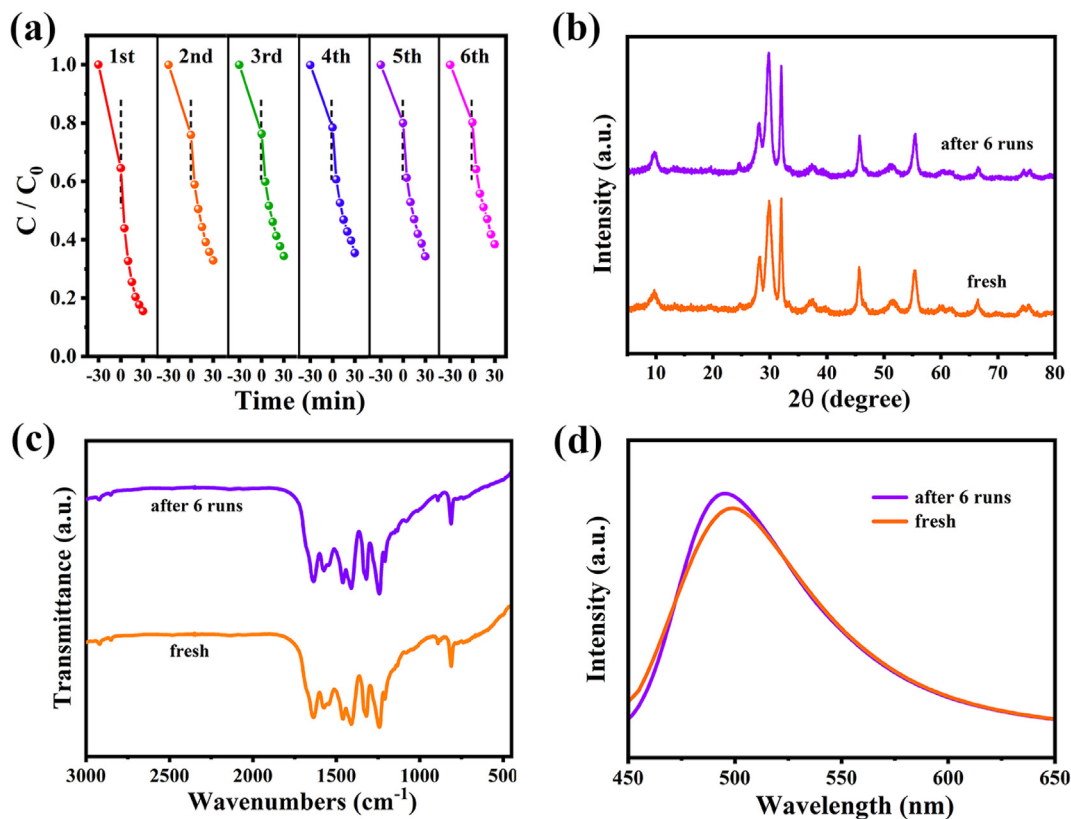


Fig. 6. (a) Recycling stability tests of BiOI/ECN-0.4 for tetracycline degradation. (b) XRD patterns, (c) FT-IR spectra, and (d) photoluminescence (PL) emission spectra of BiOI/ECN-0.4 before and after six runs.

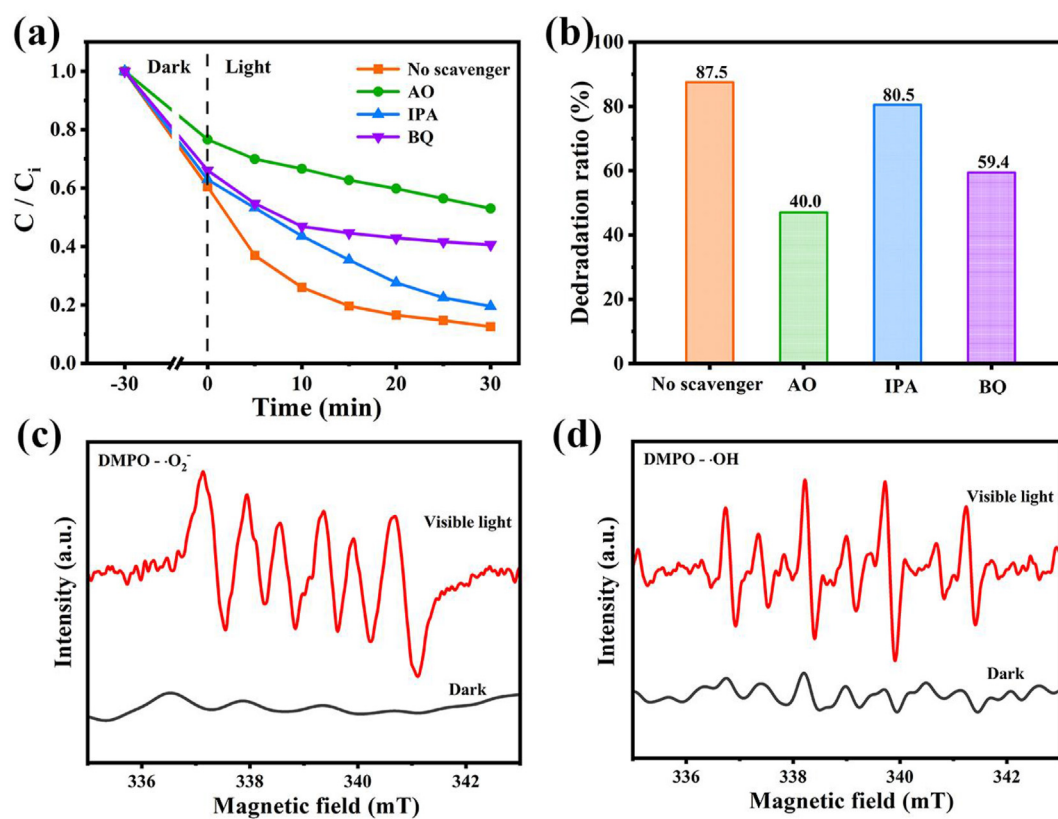


Fig. 7. Trapping experiments of active species during the photocatalytic degradation of tetracycline over BiOI/ECN-0.4 photocatalyst: (a) degradation curves; and (b) the corresponding photocatalytic removal efficiency. ESR spectra of (c) DMPO- $\bullet\text{O}_2^-$ and (d) DMPO- $\bullet\text{OH}$.

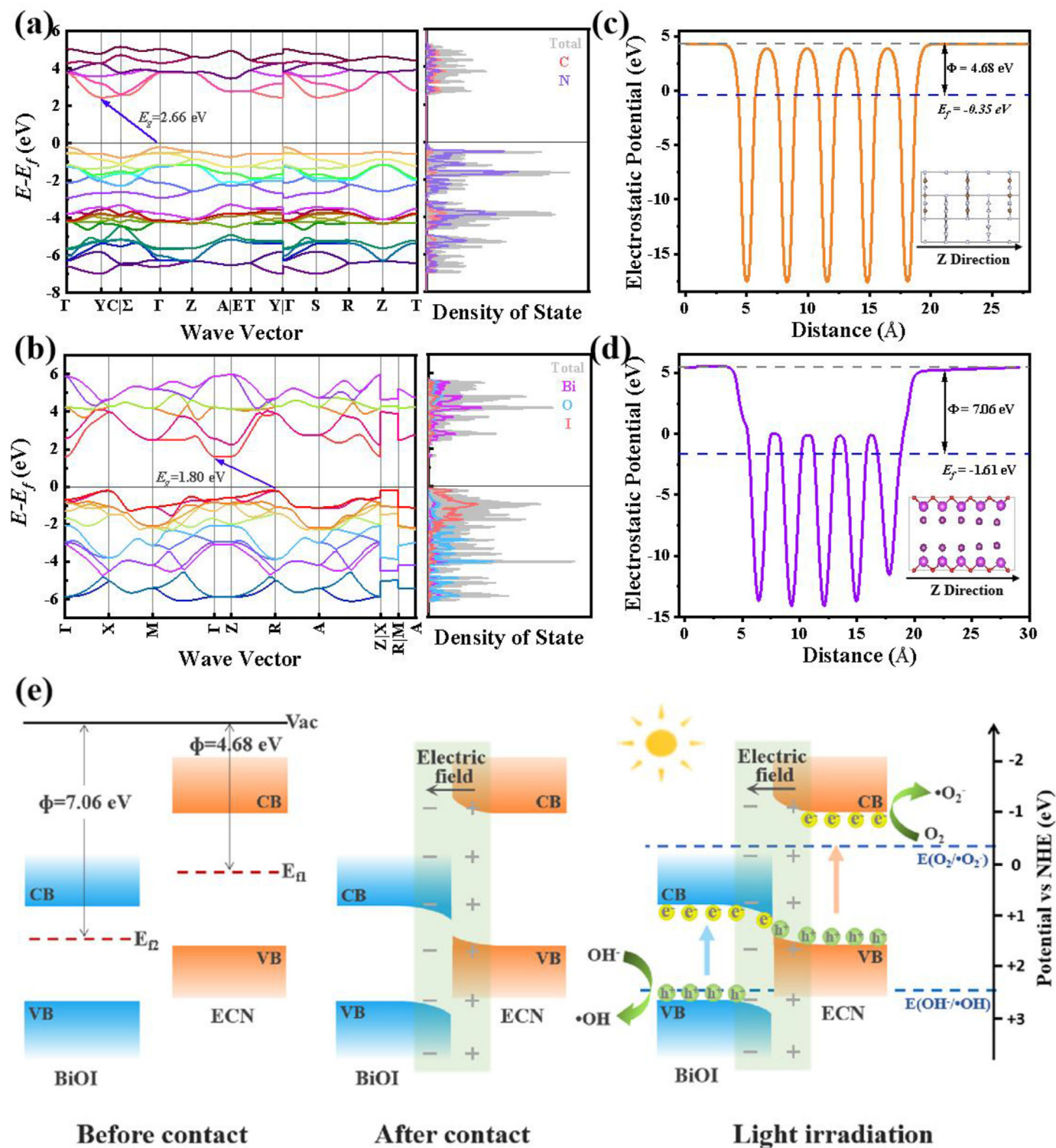


Fig. 8. The calculated band structures and the density of states (DOS) of (a) g-C₃N₄ and (b) BiOI. Calculated electrostatic potentials along Z-axis direction of (c) g-C₃N₄ and (d) BiOI. (e) The interface band bending and interfacial electron transfer diagrams between ECN and BiOI before and after contact and under light irradiation.

further certified by the ESR technique. As indicated in Fig. 7c–d, no characteristic peaks appear in the dark state. However, the characteristic signal peaks of DMPO-OH and DMPO-O₂ can be obviously found under light condition [59,60].

DFT calculation was used to calculate the band structures and DOS of photocatalysts for explaining the photocatalytic mechanism

in depth. As shown in Fig. 8a and b, the CB minimum (CBM) and VB maximum (VBM) value are located at different Γ points, indicating that g-C₃N₄ and BiOI are indirect band gap semiconductors. The calculated band gap energy (E_g) is 2.66 and 1.80 eV, respectively, which are basically in accordance with the experimentally calculated value (Fig. 3b). Combining the ECN and BiOI band gaps

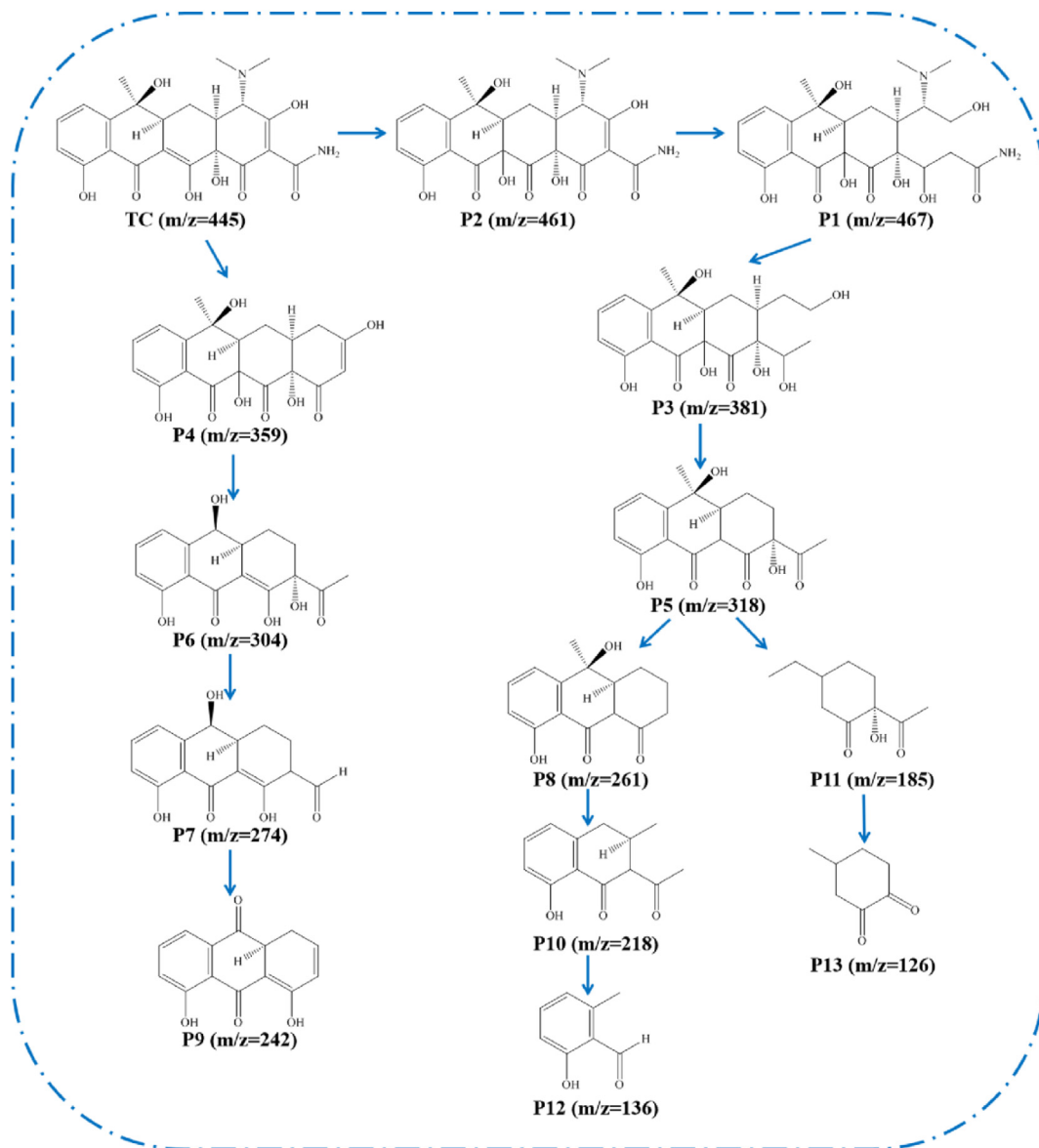


Fig. 9. The proposed photocatalytic degradation pathways of tetracycline (TC) by BiOI/ECN-0.4 photocatalyst under visible light irradiation.

obtained from the UV–vis absorption spectrum, the following empirical equations are used to estimate the band edge positions of semiconductor [15].

$$E_{CB} = X - E^e - 0.5E_g \quad (1)$$

$$E_{VB} = E_{CB} + E_g \quad (2)$$

where E_{CB} , E_{VB} , E^e , X , and E_g are the potential of conduction band (CB), the potential of valence band (VB), the energy of free electrons on the hydrogen scale (around 4.5 eV), the electronegativity, and the band gap of semiconductor, respectively. The X value is 4.73 eV for $g\text{-C}_3\text{N}_4$ and 6.21 eV for BiOI [61,62]. Hence, the E_{CB} of ECN and BiOI are determined to be -1.12 eV and 0.76 eV, whereas the E_{VB} were 1.58 eV and 2.66 eV, respectively. In the type II heterojunction structure of BiOI/ECN composite, the photogenerated electrons on the CB of ECN would move to BiOI, whereas the holes on the VB of BiOI would transfer to ECN. However, the photogenerated electrons

accumulated on the CB of BiOI could not reduce O_2 to $\cdot\text{O}_2^-$ because the E_{CB} value of BiOI is more positive than the potential of $\text{O}_2/\cdot\text{O}_2^-$ (-0.33 vs. NHE [15]). However, the previously mentioned results can not fit the free radical capture experiments and ESR testing. On the basis of previously mentioned discussion, it is proposed that the carrier transport mechanism in a BiOI/ECN composite follows the Z-scheme heterojunction.

The difference in work function between the two semiconductors is a prerequisite for inducing charge redistribution and forming an internal electric field. Fig. 8c and d show the calculated surface work functions of $g\text{-C}_3\text{N}_4$ and BiOI at circa 4.68 eV and 7.06 eV, respectively. Thus, after coupling them together, electrons in $g\text{-C}_3\text{N}_4$ would spontaneously flow to BiOI until their Fermi levels reach the same energy level [63]. Consequently, $g\text{-C}_3\text{N}_4$ is positively charged owing to the loss of electrons, and its band edge bends upward, whereas the accumulation of electrons makes BiOI negatively charged and the band edge bends downward near the contact interface. Meanwhile, this causes an internal electric field to be set up from $g\text{-C}_3\text{N}_4$ toward BiOI. Under the light condition, the local

electric field and band bending are conducive to the recombination of the photoexcited electrons in the CB of $g\text{-C}_3\text{N}_4$ with h^+ in the VB of BiOI, effectively promoting the electron-hole pair's separation. In this way, the photoinduced electrons accumulated on the CB of $g\text{-C}_3\text{N}_4$ with strong reducing ability to form $\cdot\text{O}_2^-$, whereas BiOI with higher VB potentials ($E_{\text{VB}} = 2.66$ eV) could turn OH^- into reactive $\cdot\text{OH}$ ($E(\text{OH}^-/\cdot\text{OH}) = 2.40$ eV vs. NHE [15,33]). Meanwhile, the holes accumulated on the surface of BiOI could directly participate in the oxidative degradation. The phenomenon is in well agreement with other systems that have been reported [64–66]. Photocurrent carrier migration follows the Z-scheme charge transfer mechanism between BiOI/ECN composites.

3.7. Determination of degradation pathway of TC

It is necessary to identify the photocatalytic-generated TC intermediates and evaluate their toxicity in the photocatalytic purification of the aquatic environment. On the basis of the LC-MS spectra of reaction solution (ESI, Fig. S3) and related literature reports, the structures of the main products were speculated and given in Table S1. Fig. 9 proposes the possible pathways for BiOI/ECN-0.4 photocatalyst to degrade TC. Generally, functional groups such as double bonds, phenolic groups, and amine groups are preferentially destroyed because of their relatively high electron density [67]. The double bond has higher reactivity among them; thus, TC molecule might take place hydroxylation to produce the primary product P2 ($m/z = 461$) that was changed to product P1 ($m/z = 467$) by ring-opening process. Considering the weak binding energy of N–C [33], product P4 ($m/z = 359$) and P3 ($m/z = 381$) were generated via N-demethylation and deamidation process. After that, the product P4 was demethylated, and the $\text{CH}_2\text{C}(\text{OH})$ was removed at the same time to produce the product P6 ($m/z = 304$). This process is similar to that previously reported [68]. As the reaction continued, the product P7 ($m/z = 274$) and P9 ($m/z = 242$) appeared. Meanwhile, the m/z of 318 (P5) was

transformed by P3 via the dealkylation and oxidation. With the progress of dealkylation, dihydroxylation, and ring-opening reactions, products such as P8 ($m/z = 261$), P10 ($m/z = 218$), P11 ($m/z = 185$), P12 ($m/z = 136$), and P13 ($m/z = 126$) were gradually formed. The result illustrated that the TC molecules would be gradually oxidized and destroyed to small molecules as the photocatalytic reaction went on.

3.8. Toxicity evaluation

Biological toxicity may not decrease with the increment of sequences in degradation pathways as some intermediates may exhibit higher toxicity than the original pollutant. In this study, we have evaluated the toxicity of TC and the possible degradation products from acute toxicity, bioconcentration factor, developmental toxicity, and mutagenicity (Fig. 10). The quantitative QSAR method was used to calculate the values of these parameters through Toxicity Estimation Software Tool (T.E.S.T.) [37,69]. The acute toxicity LD_{50} of P1 and P11 as well as the mutagenicity of P9 cannot be found in the database. As displayed in Fig. 10a, TC is defined as “very toxic.” Apart from P1, P6, and P8, the acute toxicity LD_{50} of the other products has been reduced. The most worrying thing is that the bioconcentration factors of most intermediates had increased significantly (Fig. 10b). Furthermore, the developmental toxicity of multiple intermediates was reduced, and some even became “developmental non-toxic” (Fig. 10c). As displayed in Fig. 10d, the mutagenicity of the products was also assessed, and it could be seen that nearly half of the products changed into “mutagenic negative.” The previously mentioned calculation results illustrated that the toxicity of the intermediates produced by the degradation of TC was reduced in some respects. However, it should not be ignored that some products still had certain toxicity in the aquatic environment. Therefore, in the process of photocatalytic degradation, it may be necessary to extend the treatment time appropriately to achieve full mineralization.

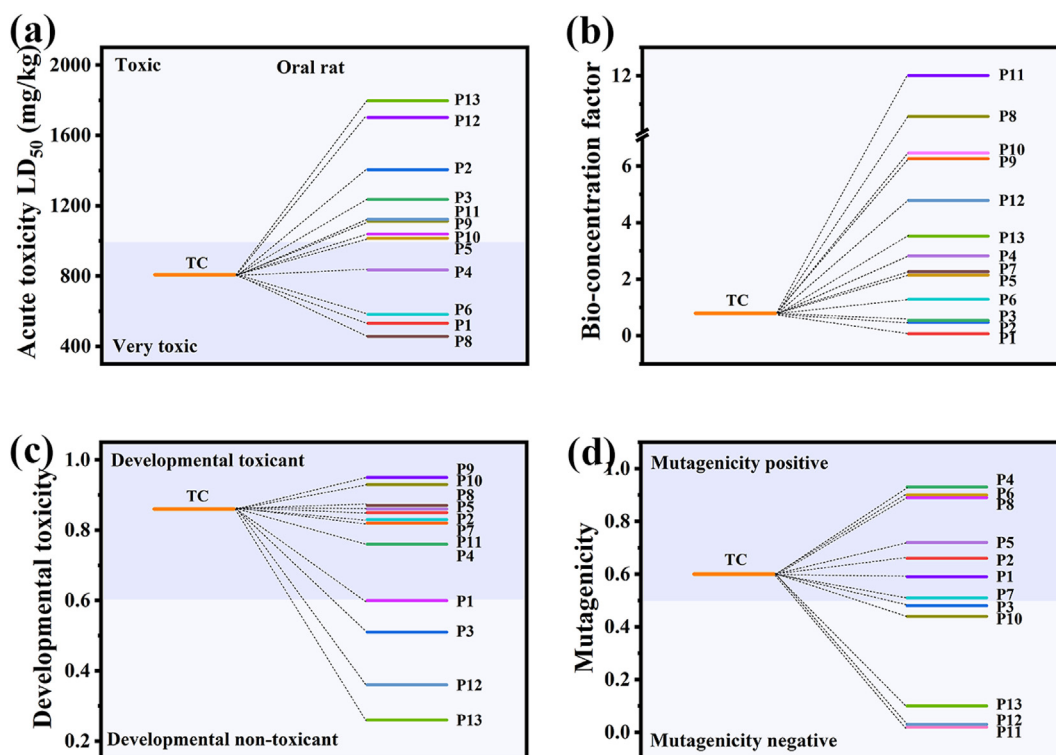


Fig. 10. Toxicity assessment of tetracycline and its possible degradation intermediates during the photocatalytic degradation of tetracycline over BiOI/ECN-0.4 photocatalyst. (a) Acute toxicity LD_{50} , (b) bioconcentration factor, (c) developmental toxicity, and (d) mutagenicity.

4. Conclusions

In summary, we successfully synthesized an innovative Z-scheme heterojunction of BiOI/ECN photocatalyst and have proved its effectiveness as a photocatalyst for TC degradation. The BiOI/ECN-0.4 delivered an optimal efficiency with 86.0% removal of TC at initial concentration of 20 mg/L in 30 min under visible light irradiation. In addition, its pseudo-first-order reaction rate constant at 0.0705 min^{-1} was nearly higher by 10 times and two times than that of bulk g-C₃N₄ and ECN, respectively. The presence of BiOI improved the adsorption capacity of the catalyst, separation of photogenerated carriers, as well as the tuned band structure, and thus, enhanced photocatalytic activity. Furthermore, the study of coexisting ions showed that CO₃²⁻ and SO₄²⁻ had a noticeable inhibitory effect. There was no significant difference in the efficiency of photocatalytic degradation of TC in a large initial pH range. Moreover, the photocatalyst exhibited great chemical stability and displayed excellent photocatalytic activity even after six reuses. DFT calculation and free radical trapping experimental results proved that the charges transfer mechanism followed the Z-scheme heterojunction structure. The results of QSAR prediction showed that the toxicity of some degradation intermediates of TC can be reduced to a lower level. This work could not only deepen the research on the process of photocatalytic degradation of TC but also provide a promising photocatalyst for the removal of antibiotic pollutants.

Authors' contributions

Hui Liu: Experimental data collection, writing the original article, methodology, and formal analysis. Wangchen Huo: Methodology, simulation, and formal analysis. Tian C. Zhang: Reviewing and editing the article. Like Ouyang: Supervision. Shaojun Yuan: Funding acquisition, supervision, project administration, and reviewing and editing the article.

Declaration of competing interest

The authors declare that they have no known competing financial interests or personal relationships that could have appeared to influence the work reported in this paper.

Acknowledgments

The authors are extremely appreciative of the National Key Research and Development Project of China (2019YFC1906404) and Open Fund of Key Laboratory of Icing and Anti/De-icing (Grant No. IADL20190305) for funding this study. The authors are also grateful for Dr. Xiang Lin, Dr. Ji Li, Mr Yuanlong Wang, and Dr. Wei Jiang from the Engineering Teaching Center, School of Chemical Engineering, Sichuan University for the FT-IR, Zeta potential, ESR, TEM and LC-MS characterization, Mr Zhang San from the Shiyanjia Lab (<http://www.shiyanjia.com>) for TEM imaging and XPS measurements, and Dr. Yingming Zhu from the Institute of New Energy and Low Carbon Technology, Sichuan University, for XRD, UV-vis DRS and SEM characterizations.

Appendix A. Supplementary data

Supplementary data to this article can be found online at <https://doi.org/10.1016/j.mtchem.2021.100729>.

References

- [1] Y. Hong, C. Li, B. Yin, D. Li, Z. Zhang, B. Mao, W. Fan, W. Gu, W. Shi, Promoting visible-light-induced photocatalytic degradation of tetracycline by an efficient and stable beta-Bi₂O₃@g-C₃N₄ core/shell nanocomposite, *Chem. Eng. J.* 338 (2018) 137–146.
- [2] S. Leong, D. Li, K. Hapgood, X. Zhang, H. Wang, Ni(OH)₂ decorated rutile TiO₂ for efficient removal of tetracycline from wastewater, *Appl. Catal. B Environ.* 198 (2016) 224–233.
- [3] C. Li, S. Yu, H. Dong, C. Liu, H. Wu, H. Che, G. Chen, Z-scheme mesoporous photocatalyst constructed by modification of Sn₃O₄ nanoclusters on g-C₃N₄ nanosheets with improved photocatalytic performance and mechanism insight, *Appl. Catal. B Environ.* 238 (2018) 284–293.
- [4] P.K. Jjemba, Excretion and ecotoxicity of pharmaceutical and personal care products in the environment, *Ecotoxicol. Environ. Saf.* 63 (2006) 113–130.
- [5] Q. Zhou, M.C. Zhang, C.D. Shuang, Z.Q. Li, A.M. Li, Preparation of a novel magnetic powder resin for the rapid removal of tetracycline in the aquatic environment, *Chin. Chem. Lett.* 23 (2012) 745–748.
- [6] W.-R. Chen, C.-H. Huang, Adsorption and transformation of tetracycline antibiotics with aluminum oxide, *Chemosphere* 79 (2010) 779–785.
- [7] I. Koyuncu, O.A. Arıkan, M.R. Wiesner, C. Rice, Removal of hormones and antibiotics by nanofiltration membranes, *J. Membr. Sci.* 309 (2008) 94–101.
- [8] R. Khan, P. Bhawana, M.H. Fulekar, Microbial decolorization and degradation of synthetic dyes: a review, *Rev. Environ. Sci. Biotechnol.* 12 (2013) 75–97.
- [9] H. Wang, Y. Wu, M. Feng, W. Tu, T. Xiao, T. Xiong, H. Ang, X. Yuan, J.W. Chew, Visible-light-driven removal of tetracycline antibiotics and reclamation of hydrogen energy from natural water matrices and wastewater by polymeric carbon nitride foam, *Water Res.* 144 (2018) 215–225.
- [10] D. Li, W. Shi, Recent developments in visible-light photocatalytic degradation of antibiotics, *Chin. J. Catal.* 37 (2016) 792–799.
- [11] D. Jiang, T. Wang, Q. Xu, D. Li, S. Meng, M. Chen, Perovskite oxide ultrathin nanosheets/g-C₃N₄ 2D-2D heterojunction photocatalysts with significantly enhanced photocatalytic activity towards the photodegradation of tetracycline, *Appl. Catal. B Environ.* 201 (2017) 617–628.
- [12] I. Papailias, N. Todorova, T. Giannakopoulou, N. Ioannidis, N. Boukos, C.P. Athanasekou, D. Dimotikali, C. Trapalis, Chemical vs thermal exfoliation of g-C₃N₄ for NO_x removal under visible light irradiation, *Appl. Catal. B Environ.* 239 (2018) 16–26.
- [13] I. Krivtsov, E.I. García-López, G. Marcí, L. Palmisano, Z. Amghouz, J.R. García, S. Ordóñez, E. Díaz, Selective photocatalytic oxidation of 5-hydroxymethyl-2-furfural to 2,5-furandicarboxyaldehyde in aqueous suspension of g-C₃N₄, *Appl. Catal. B Environ.* 204 (2017) 430–439.
- [14] J. Xiao, Y. Wang, T.C. Zhang, S. Yuan, rGO/N-porous carbon composites for enhanced CO₂ capture and energy storage performances, *J. Alloys Compd.* 857 (2021) 157534.
- [15] F. Chen, Q. Yang, Y. Wang, J. Zhao, D. Wang, X. Li, Z. Guo, H. Wang, Y. Deng, C. Niu, G. Zeng, Novel ternary heterojunction photocatalyst of Ag nanoparticles and g-C₃N₄ nanosheets co-modified BiVO₄ for wider spectrum visible-light photocatalytic degradation of refractory pollutant, *Appl. Catal. B Environ.* 205 (2017) 133–147.
- [16] Y. Wang, R. Shi, J. Lin, Y. Zhu, Enhancement of photocurrent and photocatalytic activity of ZnO hybridized with graphite-like C₃N₄, *Energy Environ. Sci.* 4 (2011).
- [17] S. Cao, J. Low, J. Yu, M. Jaroniec, Polymeric photocatalysts based on graphitic carbon nitride, *Adv. Mater.* 27 (2015) 2150–2176.
- [18] J. Di, J. Xia, Y. Ge, L. Xu, H. Xu, M. He, Q. Zhang, H. Li, Reactable ionic liquid-assisted rapid synthesis of BiOI hollow microspheres at room temperature with enhanced photocatalytic activity, *J. Mater. Chem.* 2 (2014) 15864–15874.
- [19] L. Ai, Y. Zeng, J. Jiang, Hierarchical porous BiOI architectures: facile microwave nonaqueous synthesis, characterization and application in the removal of Congo red from aqueous solution, *Chem. Eng. J.* 235 (2014) 331–339.
- [20] X. Wang, S. Yang, H. Li, W. Zhao, C. Sun, H. He, High adsorption and efficient visible-light-photodegradation for cationic Rhodamine B with microspheric BiOI photocatalyst, *RSC Adv.* 4 (2014) 42530–42537.
- [21] S. Wang, Y. Guan, L. Wang, W. Zhao, H. He, J. Xiao, S. Yang, C. Sun, Fabrication of a novel bifunctional material of BiOI/Ag₃VO₄ with high adsorption-photocatalysis for efficient treatment of dye wastewater, *Appl. Catal. B Environ.* 168–169 (2015) 448–457.
- [22] H. Feng, L. Liang, Y. Liu, Z. Huang, L. Li, Efficient nano-regional photocatalytic heterostructure design via the manipulation of reaction site self-quenching effect, *Appl. Catal. B Environ.* 243 (2019) 220–228.
- [23] J.H. Zhu, Y.G. Feng, A.J. Wang, L.P. Mei, X. Luo, J.J. Feng, A signal-on photoelectrochemical aptasensor for chloramphenicol assay based on 3D self-supporting AgI/Ag/BiOI Z-scheme heterojunction arrays, *Biosens. Bioelectron.* 181 (2021) 113158.
- [24] X. Jiang, S. Lai, W. Xu, J. Fang, X. Chen, J. Beiyuan, X. Zhou, K. Lin, J. Liu, G. Guan, Novel ternary BiOI/g-C₃N₄/CeO₂ catalysts for enhanced photocatalytic degradation of tetracycline under visible-light radiation via double charge transfer process, *J. Alloys Compd.* 809 (2019) 151804.
- [25] Y. Cui, L. Yang, J. Zheng, Z. Wang, B. Li, Y. Yan, M. Meng, Synergistic interaction of Z-scheme 2D/3D g-C₃N₄/BiOI heterojunction and porous PVDF membrane for greatly improving the photodegradation efficiency of tetracycline, *J. Colloid Interface Sci.* 586 (2021) 335–348.

- [26] G. Kresse, J. Furthmüller, Efficient iterative schemes for ab initio total-energy calculations using a plane-wave basis set, *Phys. Rev. B* 54 (1996) 11169–11186.
- [27] P.E. Blöchl, Projector augmented-wave method, *Phys. Rev. B* 50 (1994) 17953–17979.
- [28] J.P. Perdew, K. Burke, M. Ernzerhof, Generalized gradient approximation made simple, *Phys. Rev. Lett.* 77 (1996) 3865–3868.
- [29] V. Wang, N. Xu, J.-C. Liu, G. Tang, W.-T. Geng, VASPKIT: a user-friendly interface facilitating high-throughput computing and analysis using VASP code, *Comput. Phys. Commun.* 267 (2021) 108033.
- [30] S. Grimme, S. Ehrlich, L. Goerigk, Effect of the damping function in dispersion corrected density functional theory, *J. Comput. Chem.* 32 (2011) 1456–1465.
- [31] S. Grimme, J. Antony, S. Ehrlich, H. Krieg, A consistent and accurate ab initio parametrization of density functional dispersion correction (DFT-D) for the 94 elements H–Pu, *J. Chem. Phys.* 132 (2010) 154104.
- [32] J. Heyd, G.E. Scuseria, Assessment and validation of a screened Coulomb hybrid density functional, *J. Chem. Phys.* 120 (2004) 7274–7280.
- [33] L. Tang, C. Feng, Y. Deng, G. Zeng, J. Wang, Y. Liu, H. Feng, J. Wang, Enhanced photocatalytic activity of ternary Ag/g-C₃N₄/NaTaO₃ photocatalysts under wide spectrum light radiation: the high potential band protection mechanism, *Appl. Catal. B Environ.* 230 (2018) 102–114.
- [34] P. Niu, L. Zhang, G. Liu, H.M. Cheng, Graphene-like carbon nitride nanosheets for improved photocatalytic activities, *Adv. Funct. Mater.* 22 (2012) 4763–4770.
- [35] Y. Li, M.Q. Wang, S.J. Bao, S. Lu, M. Xu, D. Long, S. Pu, Tuning and thermal exfoliation graphene-like carbon nitride nanosheets for superior photocatalytic activity, *Ceram. Int.* 42 (2016) 18521–18528.
- [36] J. Xiao, Y. Xie, F. Nawaz, S. Jin, F. Duan, M. Li, H. Cao, Super synergy between photocatalysis and ozonation using bulk g-C₃N₄ as catalyst: a potential sunlight/O₃/g-C₃N₄ method for efficient water decontamination, *Appl. Catal. B Environ.* 181 (2016) 420–428.
- [37] Y. Wang, L. Rao, P. Wang, Z. Shi, L. Zhang, Photocatalytic activity of N-TiO₂/O-doped N vacancy g-C₃N₄ and the intermediates toxicity evaluation under tetracycline hydrochloride and Cr(VI) coexistence environment, *Appl. Catal. B Environ.* (2020) 262.
- [38] J. Xiao, Y. Wang, T.C. Zhang, S. Yuan, N,S-containing polycondensate-derived porous carbon materials for superior CO₂ adsorption and supercapacitor, *Appl. Surf. Sci.* 562 (2021) 150128.
- [39] J. Ji, H. He, C. Chen, W. Jiang, A. Raza, T.J. Zhang, S. Yuan, Biomimetic hierarchical TiO₂@CuO nanowire arrays-coated copper meshes with superwetting and self-cleaning properties for efficient oil/water separation, *ACS Sustain. Chem. Eng.* 7 (2018) 2569–2577.
- [40] C. Chang, L. Zhu, S. Wang, X. Chu, L. Yue, Novel mesoporous graphite carbon nitride/BiOI heterojunction for enhancing photocatalytic performance under visible-light irradiation, *ACS Appl. Mater. Interfaces* 6 (2014) 5083–5093.
- [41] C. Yu, J.C. Yu, C. Fan, H. Wen, S. Hu, Synthesis and characterization of Pt/BiOI nanoplate catalyst with enhanced activity under visible light irradiation, *Mater. Sci. Eng., B* 166 (2010) 213–219.
- [42] C. Chang, L. Zhu, Y. Fu, X. Chu, Highly active Bi/BiOI composite synthesized by one-step reaction and its capacity to degrade bisphenol A under simulated solar light irradiation, *Chem. Eng. J.* 233 (2013) 305–314.
- [43] N. Tian, H. Huang, S. Wang, T. Zhang, X. Du, Y. Zhang, Facet-charge-induced coupling dependent interfacial photocharge separation: a case of BiOI/g-C₃N₄ p-n junction, *Appl. Catal. B Environ.* 267 (2020).
- [44] J.C. Wang, H.C. Yao, Z.Y. Fan, L. Zhang, J.S. Wang, S.Q. Zang, Z.J. Li, Indirect Z-scheme BiOI/g-C₃N₄ photocatalysts with enhanced photoreduction CO₂ activity under visible light irradiation, *ACS Appl. Mater. Interfaces* 8 (2016) 3765–3775.
- [45] J. Wen, J. Xie, Z. Yang, R. Shen, H. Li, X. Luo, X. Chen, X. Li, Fabricating the robust g-C₃N₄ nanosheets/carbons/NiS multiple heterojunctions for enhanced photocatalytic H₂ generation: an insight into the trifunctional roles of nanocarbons, *ACS Sustain. Chem. Eng.* 5 (2017) 2224–2236.
- [46] X. Yuan, C. Zhou, Y. Jin, Q. Jing, Y. Yang, X. Shen, Q. Tang, Y. Mu, A.K. Du, Facile synthesis of 3D porous thermally exfoliated g-C₃N₄ nanosheet with enhanced photocatalytic degradation of organic dye, *J. Colloid Interface Sci.* 468 (2016) 211–219.
- [47] M. Kong, Y. Li, X. Chen, T. Tian, P. Fang, F. Zheng, X. Zhao, Tuning the relative concentration ratio of bulk defects to surface defects in TiO₂ nanocrystals leads to high photocatalytic efficiency, *J. Am. Chem. Soc.* 133 (2011) 16414–16417.
- [48] H. Che, C. Liu, W. Hu, H. Hu, J. Li, J. Dou, W. Shi, C. Li, H. Dong, NGQD active sites as effective collectors of charge carriers for improving the photocatalytic performance of Z-scheme g-C₃N₄/Bi₂WO₆ heterojunctions, *Catal. Sci. Technol.* 8 (2018) 622–631.
- [49] J. Xiao, Y. Wang, T.C. Zhang, L. Ouyang, S. Yuan, Phytic acid-induced self-assembled chitosan gel-derived N, P-co-doped porous carbon for high-performance CO₂ capture and supercapacitor, *J. Power Sources* 517 (2022) 230727.
- [50] X. Hu, C. Hu, Preparation and visible-light photocatalytic activity of Ag₃VO₄ powders, *J. Solid State Chem.* 180 (2007) 725–732.
- [51] S. Naraginti, Y.Y. Yu, Z. Fang, Y.C. Yong, Novel tetrahedral Ag₃PO₄@N-rGO for photocatalytic detoxification of sulfamethoxazole: process optimization, transformation pathways and biotoxicity assessment, *Chem. Eng. J.* 375 (2019) 122035.
- [52] X. Zhong, K.X. Zhang, D. Wu, X.Y. Ye, W. Huang, B.X. Zhou, Enhanced photocatalytic degradation of levofloxacin by Fe-doped BiOI nanosheets under LED light irradiation, *Chem. Eng. J.* 383 (2020) 123148.
- [53] G.H. Safari, M. Hoseini, M. Seyedsalehi, H. Kamani, J. Jaafari, A.H. Mahvi, Photocatalytic degradation of tetracycline using nanosized titanium dioxide in aqueous solution, *Int. J. Environ. Sci. Technol.* 12 (2014) 603–616.
- [54] Y. Zhang, D. Jiang, Y. Wang, T.C. Zhang, G. Xiang, Y.X. Zhang, S. Yuan, Core-shell structured magnetic γ-Fe₂O₃@PANI nanocomposites for enhanced As(V) adsorption, *Ind. Eng. Chem. Res.* 59 (2020) 7554–7563.
- [55] Y. Zhao, X. Gu, S. Gao, J. Geng, X. Wang, Adsorption of tetracycline (TC) onto montmorillonite: cations and humic acid effects, *Geoderma* 183–184 (2012) 12–18.
- [56] F. Saadati, N. Keramati, M.M. Ghazi, Influence of parameters on the photocatalytic degradation of tetracycline in wastewater: a review, *Crit. Rev. Environ. Sci. Technol.* 46 (2016) 757–782.
- [57] C. Du, Z. Zhang, S. Tan, G. Yu, H. Chen, L. Zhou, L. Yu, Y. Su, Y. Zhang, F. Deng, S. Wang, Construction of Z-scheme g-C₃N₄/MnO₂/GO ternary photocatalyst with enhanced photodegradation ability of tetracycline hydrochloride under visible light radiation, *Environ. Res.* 200 (2021) 111427.
- [58] J. Cao, Z.H. Yang, W.P. Xiong, Y.Y. Zhou, Y.R. Peng, X. Li, C.Y. Zhou, R. Xu, Y.R. Zhang, One-step synthesis of Co-doped UiO-66 nanoparticle with enhanced removal efficiency of tetracycline: simultaneous adsorption and photocatalysis, *Chem. Eng. J.* 353 (2018) 126–137.
- [59] X. Liu, Y. Wang, T.C. Zhang, G. Xiang, X. Wang, S. Yuan, One-pot synthesis of a magnetic TiO₂/PTh/γ-Fe₂O₃ heterojunction nanocomposite for removing trace arsenite via simultaneous photocatalytic oxidation and adsorption, *Ind. Eng. Chem. Res.* 60 (2020) 528–540.
- [60] Y. Wang, Y. Zhang, T.C. Zhang, G. Xiang, X. Wang, S. Yuan, Removal of trace arsenite through simultaneous photocatalytic oxidation and adsorption by magnetic Fe₃O₄@PpPDA@TiO₂ core-shell nanoparticles, *ACS Appl. Nano Mater.* 3 (2020) 8495–8504.
- [61] H. Dong, X. Zhang, J. Li, P. Zhou, S. Yu, N. Song, C. Liu, G. Che, C. Li, Construction of morphology-controlled nonmetal 2D/3D homojunction towards enhancing photocatalytic activity and mechanism insight, *Appl. Catal. B Environ.* (2020) 263.
- [62] H. Wang, H. Ye, B. Zhang, F. Zhao, B. Zeng, Electrostatic interaction mechanism based synthesis of a Z-scheme BiOI–CdS photocatalyst for selective and sensitive detection of Cu²⁺, *J. Mater. Chem.* 5 (2017) 10599–10608.
- [63] T. Jia, J. Wu, Y. Xiao, Q. Liu, Q. Wu, Y. Qi, X. Qi, Self-grown oxygen vacancies-rich CeO₂/BiOBr Z-scheme heterojunction decorated with rGO as charge transfer channel for enhanced photocatalytic oxidation of elemental mercury, *J. Colloid Interface Sci.* 587 (2021) 402–416.
- [64] Y. Jia, Z. Wang, X.Q. Qiao, L. Huang, S. Gan, D. Hou, J. Zhao, C. Sun, D.S. Li, A synergistic effect between S-scheme heterojunction and Noble-metal free cocatalyst to promote the hydrogen evolution of ZnO/CdS/MoS₂ photocatalyst, *Chem. Eng. J.* 424 (2021).
- [65] C. Liang, H.P. Feng, H.Y. Niu, C.G. Niu, J.S. Li, D.W. Huang, L. Zhang, H. Guo, N. Tang, H.Y. Liu, A dual transfer strategy for boosting reactive oxygen species generation in ultrathin Z-scheme heterojunction driven by electronic field, *Chem. Eng. J.* 384 (2020).
- [66] Y. Jia, S. Li, J. Gao, G. Zhu, F. Zhang, X. Shi, Y. Huang, C. Liu, Highly efficient (BiO)₂CO₃-BiO₂-x-graphene photocatalysts: Z-Scheme photocatalytic mechanism for their enhanced photocatalytic removal of NO, *Appl. Catal. B Environ.* 240 (2019) 241–252.
- [67] J. Wang, D. Zhi, H. Zhou, X. He, D. Zhang, Evaluating tetracycline degradation pathway and intermediate toxicity during the electrochemical oxidation over a Ti/Ti₄O₇ anode, *Water Res.* 137 (2018) 324–334.
- [68] M. Zhou, D. Han, X. Liu, C. Ma, H. Wang, Y. Tang, P. Huo, W. Shi, Y. Yan, J. Yang, Enhanced visible light photocatalytic activity of alkaline earth metal ions-doped CdSe/rGO photocatalysts synthesized by hydrothermal method, *Appl. Catal. B Environ.* 172–173 (2015) 174–184.
- [69] W. Liu, Y. Li, F. Liu, W. Jiang, D. Zhang, J. Liang, Visible-light-driven photocatalytic degradation of diclofenac by carbon quantum dots modified porous g-C₃N₄: mechanisms, degradation pathway and DFT calculation, *Water Res.* 151 (2019) 8–19.